A coupled three dimensional model of vanadium redox flow battery for flow field designs

Cong Yin [a, b], Yan Gao [b], Shaoyun Guo [a], Hao Tang [b, *]

[a] The State Key Laboratory of Polymer Materials Engineering, Polymer Research Institute of Sichuan University, Chengdu 610065, China
[b] Energy Conversion R&D Center, Central Academy of Dongfang Electric Corporation, Chengdu 611731, China

A B S T R A C T

A 3D (three-dimensional) model of VRB (vanadium redox flow battery) with interdigitated flow channel design is proposed. Two different stack inlet designs, single-inlet and multi-inlet, are structured in the model to study the distributions of fluid pressure, electric potential, current density and overpotential during operation of VRB cell. Electrolyte flow rate and stack channel dimension are proved to be the critical factors affecting flow distribution and cell performance. The model developed in this paper can be employed to optimize both VRB stack design and system operation conditions. Further improvements of the model concerning current density and electrode properties are also suggested in the paper.

© 2014 Elsevier Ltd. All rights reserved.

1. Introduction

ESS (Energy Storage System) technology based on electrochemical reactors is getting more attention in R&D and product commercialization [1—14]. VRB (Vanadium redox flow battery) system, with its advantages of high energy efficiency, long cycle life and flexible capacity design, is one of the promising ESS technologies for storage of renewable energy and stabilization of local grid electricity supplies [1—9]. Several VRB systems have been installed for product demonstration and field trials. However, their performance, lifetime and efficiency need to be improved significantly prior to VRB commercialization. Therefore, many scientists and engineers focused on fundamental studies of VRB electrochemical reactions to improve the system performance and lifetime [15—24]. Among these scientific studies, computational simulation is a powerful tool to reveal the nature of electrochemical reaction of VRB cell reactor and to save tremendous experimental work.

Over the last decade, numerical modeling of VRB system has been researched by many groups and simulations of flow-through porous electrode cell structures of VRB are discussed in detail [1,25—32]. M. Vynnycky built a 2D time-dependent single-phase isothermal model with single cell to optimize VRB operation condition [1]. A. A. Shah et al. proposed dynamic models of VRB system

and studied the effects of gas evolution, electrolyte flow rate and current density on cell performance [25—29]. While D. You investigated the effects of porous electrode thickness ratio on the current density distribution and a two-dimensional model of a single cell was developed to predict the cell performance [30]. A dynamic thermal model based on energy conservation was established by A. Tang and M. Skyllas-Kazacos to simulate the VRB stack temperature distribution characteristics with different stack structures [31].

Recently, Q. Xu et al. focused on numerical investigations of serpentine and parallel flow field designs of VRB cells and studied the cell performance for the different flow fields [32]. Compared to the two flow fields, the interdigitated flow field is a key technology to distribute electrolyte with less fluid pressure drop than the serpentine one and more efficient mass transfer than the parallel one. In this paper, a 3D stationary model of interdigitated flow field is proposed to simulate the distribution patterns of electrolyte fluid flow, cell's voltage and current density in terms of stack structure and electrolyte flow rate. Based on the simulation results, stack design parameters and operation conditions are optimized to improve both VRB performance and system efficiency.

2. Model development

2.1. Geometric model building

The theoretical model of VRB is based on a 3D single cell structure as depicted in Fig. 1, which is composed of current

---

* Corresponding author. Tel.: +86 028 87898285; fax: +86 028 87898205.
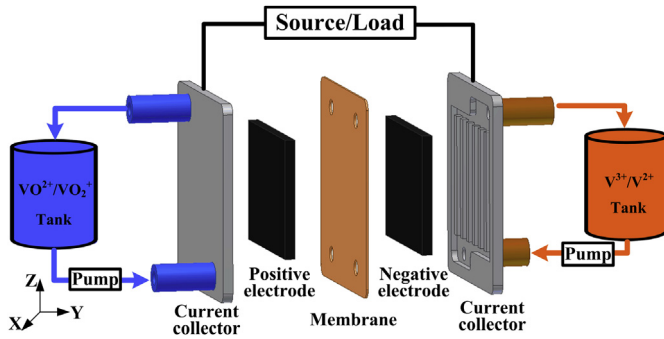 *E-mail addresses:* yincong@dongfang.com (C. Yin), tanghao@dongfang.com (H. Tang).

Fig. 1. A schematic of an all-vanadium redox flow battery system.

Table 1
Default parameters of the VRB cell's geometric structure.

Symbol	Parameter	Value
a	Channel width	1.5 mm
b	Channel height	1.5 mm
c	Land width	2 mm
d_1	Porous electrode thickness	2 mm
d_2	Membrane thickness	0.5 mm
d_3	Current collector thickness	2.5 mm
m	Width of porous electrode	7 mm
n	Length of porous electrode	10 mm

collectors, porous electrodes and a proton exchange membrane. Electrolyte solution containing vanadium ions of different valences, V^{2+}/V^{3+} for the negative electrode and VO^{2+}/VO_2^+ for the positive electrode, are circulated into the cell stack by liquid pumps respectively. The main half-reactions of the two electrodes for VRB are as follows:

Negative electrode: $V^{3+} + e^- \Leftrightarrow V^{2+}$
Positive electrode: $VO^{2+} + H_2O \Leftrightarrow VO_2^+ + 2H^+ + e^-$

As the geometric size of a regular VRB cell is too large for computational modeling, a simplified 3D model is built in this paper as shown in Fig. 2, including current collectors with inlet and outlet channels, porous electrodes for positive and negative half-cells respectively, and an ion exchange membrane to separate the two half-cells. The so-called interdigitated flow channels are depicted in Fig. 2(b), where the electrolyte solution is forced to flow through the porous electrode between the inlet and outlet channels with dead ends in the current collector. The default structural parameters of the cell model are given in Table 1.

2.2. Model assumptions

Several assumptions are applied to the present model and shown as follows:

(1) The electrolyte is considered as incompressible fluid and dilute solution when dealing with the fluid flow issues, as the volume change is too small and the ionic concentrations are sufficiently low.
(2) Side reactions such as hydrogen and oxygen evolution are not taken into account.
(3) Crossover of vanadium ions and water through the membrane is ignored.
(4) Temperature effect is neglected in the present model.

2.3. Governing equations

In order to describe the fluid flow inside the cell, the Navier–Stokes equations for incompressible fluid are used for the laminar flow in channel domains and the Brinkman equations are applied to deal with fluids in porous electrode, respectively. The momentum and continuity equations for laminar flow are as follows:

$$\rho\left(\vec{u} \cdot \nabla\right)\vec{u} = -\nabla p + \nabla \cdot \left[\mu\left(\nabla \vec{u} + (\nabla \vec{u})^T\right)\right] + \vec{f} \tag{1}$$

$$\rho \nabla \cdot \vec{u} = 0 \tag{2}$$

where ρ is the fluid density, $\vec{u}$ is the velocity, p is the pressure, $\vec{f}$ is the volume force vector and μ is the dynamic viscosity of the fluid.

And for the fluid flowing in porous media, the corresponding equations are:

$$\frac{\rho}{\varepsilon}\left(\vec{u} \cdot \nabla\right)\frac{\vec{u}}{\varepsilon} = -\nabla p + \nabla \cdot \left[\frac{\mu}{\varepsilon}\left(\nabla \vec{u} + (\nabla \vec{u})^T\right)\right] - \frac{2\mu}{3\varepsilon}\nabla(\nabla \cdot \vec{u})$$
$$- \left(\frac{\mu}{K} + Q\right)\vec{u} + \vec{f} \tag{3}$$

$$\rho \nabla \cdot \vec{u} = Q \tag{4}$$

where ε is the porosity, K is the permeability of the porous medium and Q is the mass source.

On the basis of velocity field simulation, mass balance for each species is given by the Nernst–Planck equation:
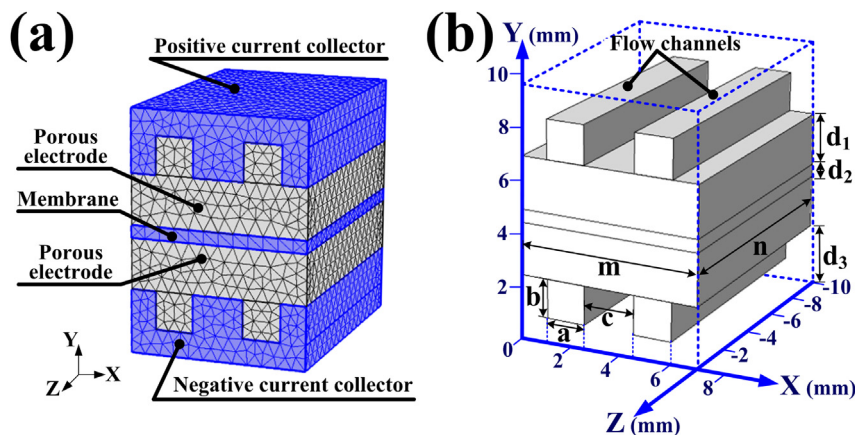

Fig. 2. The simplified 3D model of interdigitated flow channels for VRB cell composed of current collectors, porous electrodes and an ion exchange membrane. (a) The mesh building. (b) The detailed geometry.

$$\frac{\partial}{\partial t}(\varepsilon c_i) + \nabla \cdot \left(-\varepsilon^{3/2} D_i \nabla c_i - \frac{z_i c_i \varepsilon^{3/2} D_i F \nabla \Phi}{RT} + \vec{u} c_i \right) = R_i \quad (5)$$

where R_i is the source term of species i, c_i, D_i and z_i are the bulk concentration, diffusion coefficient and charge of species i, Φ is the potential, F is the Faraday's constant and R is the ideal gas constant.

As for the reversible electrochemical reactions in the porous electrodes, the transfer current densities of the positive electrode j_1 and the negative electrode j_2 are given by Butler–Volmer's law:

$$j_1 = Fk_1 \sqrt{c_4^s c_5^s} \left[\exp\left(\frac{F\eta_1}{2RT} \right) - \exp\left(-\frac{F\eta_1}{2RT} \right) \right] \quad (6)$$

$$j_2 = Fk_2 \sqrt{c_2^s c_3^s} \left[\exp\left(\frac{F\eta_2}{2RT} \right) - \exp\left(-\frac{F\eta_2}{2RT} \right) \right] \quad (7)$$

of which, c_2^s, c_3^s, c_4^s and c_5^s are the surface concentrations of V^{2+}, V^{3+}, VO^{2+} and VO_2^+ ions which are generally different from the bulk concentration c_i, k_1 and k_2 are the reaction rate constants. η_1 and η_2 represent the activation overpotentials of positive and negative reactions which are defined as:

$$\eta_1 = \Phi_s - \Phi_l - E_1 \quad (8)$$

$$\eta_2 = \Phi_s - \Phi_l - E_2 \quad (9)$$

where Φ_s and Φ_l are the electric potentials of the solid and liquid phases, E_1 and E_2 are the equilibrium potentials for the positive and negative reactions, calculated by the Nernst equations:

$$E_1 = E_1^0 + \frac{RT}{F} \ln\left(\frac{c_5}{c_4} \right) \quad (10)$$

$$E_2 = E_2^0 - \frac{RT}{F} \ln\left(\frac{c_2}{c_3} \right) \quad (11)$$

where E_1^0 and E_2^0 are the standard potentials for the positive and negative reactions at $T = 298.15$ K.

The surface concentrations c_i^s indicate the concentrations of vanadium ions at the liquid–solid interfaces in the porous electrodes, which could be estimated by the bulk concentrations c_i, average pore diameter of the porous structure d_p, diffusion coefficients D_i and rates of reactions [29].

$$c_4^s = \frac{c_4 + \varepsilon k_1 e^{-F(\Phi_s - \Phi_l - E_1^0)/(2RT)}(c_4/\gamma_5 + c_5/\gamma_4)}{1 + \varepsilon k_1 \left(e^{-F(\Phi_s - \Phi_l - E_1^0)/(2RT)} / \gamma_5 + e^{F(\Phi_s - \Phi_l - E_1^0)/(2RT)} / \gamma_4 \right)} \quad (12)$$

$$c_5^s = \frac{c_5 + \varepsilon k_1 e^{F(\Phi_s - \Phi_l - E_1^0)/(2RT)}(c_4/\gamma_5 + c_5/\gamma_4)}{1 + \varepsilon k_1 \left(e^{-F(\Phi_s - \Phi_l - E_1^0)/(2RT)} / \gamma_5 + e^{F(\Phi_s - \Phi_l - E_1^0)/(2RT)} / \gamma_4 \right)} \quad (13)$$

where $\gamma_4 = D_4/d_p$ and $\gamma_5 = D_5/d_p$. Similar expressions of c_2^s and c_3^s could be obtained for the negative electrode.

Coupled with the reaction kinetics mentioned above, the current distribution is calculated with the Ohm's law:

$$\vec{i}_1 = -\sigma_1 \nabla \Phi_l \quad (14)$$

$$\vec{i}_s = -(1-\varepsilon)^{3/2} \sigma_s \nabla \Phi_s \quad (15)$$

where $\vec{i}_1$ and $\vec{i}_s$ are the local current densities for liquid and solid phase respectively, with σ_1 and σ_s denoting the relative conductivities.

2.4. Boundary conditions

In this study, flow rate is initialized by the parameter *stoich*, which indicates the ratio of input reactants molar versus the consumed one under certain current applied, defined as:

$$stoich = \frac{uA_{inlet}Fc_0 soc}{i_{inward}A_{electrode}} \quad (16)$$

where A_{inlet} is the cross-section area of the inlet, $A_{electrode}$ is the area of the current collector, i_{inward} is the inward current density of the current collector, c_0 is the total concentration of vanadium ions and *soc* represents the state of charge of the cell given by:

$$soc = c_2^{inlet} / c_0 = c_5^{inlet} / c_0 = 1 - c_3^{inlet} / c_0 = 1 - c_4^{inlet} / c_0 \quad (17)$$

where c_2^{inlet}, c_3^{inlet}, c_4^{inlet} and c_5^{inlet} are the concentrations of V^{2+}, V^{3+}, VO^{2+} and VO_2^+ ions at the inlet.

Constant values including *soc*, ionic concentrations and inward current density of current collector, as well as other default parameters for the simulation are shown in Table 2.

2.5. Numerical details

Equations of the presented model were solved with the COMSOL Multiphysics® package using finite-element method. A quadratic basis was used in all of the simulations together with 43,308 elements for the interdigitated flow field model. The relative error tolerance was set to 1×10^{-6}.

3. Results and discussion

In this study, interdigitated flow channel models of different inlet designs are simulated to study the cell performance under varied operation conditions. The effects of inlet design, applied flow rate and channel dimension on fluid distribution pattern and cell performance are discussed.

Table 2
Parameter values for the simulation.

Symbol	Parameter	Value
D_2	V^{2+} ionic diffusion coefficient	2.4×10^{-10} m²/s [1]
D_3	V^{3+} ionic diffusion coefficient	2.4×10^{-10} m²/s [1]
D_4	V^{4+} ionic diffusion coefficient	3.9×10^{-10} m²/s [1]
D_5	V^{5+} ionic diffusion coefficient	3.9×10^{-10} m²/s [1]
D_{H_2O}	Water diffusion coefficient	2.3×10^{-9} m²/s [26]
D_{H^+}	Proton diffusion coefficient	9.31×10^{-9} m²/s [1]
k_1	Standard rate constant: positive	6.8×10^{-7} m/s [30]
k_2	Standard rate constant: negative	1.7×10^{-7} m/s [30]
E_1^0	Equilibrium potential: V^{4+}/V^{5+}	1.004 V
E_2^0	Equilibrium potential: V^{2+}/V^{3+}	−0.255 V
ε	Porosity of the electrode	0.9
d_p	Carbon fiber diameter	1.76×10^{-5} m
ρ	Density of the electrolyte	1300 kg/m³
μ	Viscosity of the electrolyte	4.928×10^{-3} Pa s
σ_s	Electronic conductivity of solid	1000 S/m
σ_1	Conductivity of electrolyte	80 S/m
σ_{mem}	Conductivity of membrane	10 S/m
T	Temperature	298 K
c_0	Total concentration of vanadium ions	1500 mol/L
soc	State of charge	0.5
i_{inward}	Applied current density	60 mA/cm²

3.1. Model validation

A single cell is assembled for the experiment of charge and discharge test as shown in Fig. 3. The carbon felt electrode area is 90 mm × 60 mm, with a thickness of 4 mm. Two PVC (polyvinyl chloride) frames are used in the cell to construct positive and negative electrode chambers which are divided by a Nafion 115 proton exchange membrane. PTFE (polytetrafluoroethylene) gaskets are applied between the adjacent cell compartments for sealing and the cell components are fastened together with four tie rods. The fluid inlets and outlets of the cell are constructed at the side of the polymer insulators with a thickness of 30 mm.

To validate the coupled 3D model, performance of the single cell with no flow channels is tested and compared with the model prediction under the same conditions. In experiment, the *soc* range for charge and discharge processes is set as 0.2 to 0.8 with a current density of 60 mA/cm^2 and the constant electrolyte flow rate is set as 6 ml/s. The comparison between the numerical and experimental data is shown in Fig. 4 and Table 3. It is seen that cell performance given by the VRB model matches the experimental results very well with less than 1% of deviation during VRB charging (*soc* 0.2−0.8) and discharging periods (*soc* 0.4−0.8). With lower discharging *soc* values (0.3 and 0.2), the deviation reaches 1.25% and 2.06%, respectively, which may be caused by ions cross-over through the membrane and side reactions which are not taken into account in the simulation. However, VRB system is rarely operated with these low *soc* values considering the balance of storage capacity and energy conversion efficiency.

3.2. Effects of inlet design on cell's distribution patterns

Two different inlet designs, single-inlet and multi-inlet, are constructed in this model as shown in Fig 5. In the single-inlet design, fluid flows through the porous electrode from the inlet channel to the outlet one. While in the multi-inlet design, one part of fluid directly goes through the cross-section of porous electrode by the side inlet and the other part of fluid follows the channel-to-channel path, of which the proportion is determined by the channel geometry. The outlet manifold designs are as same as the inlet counterparts. Both the outlet and inlet channels are dead-ended. Fig. 6 shows the pressure distribution of the electrolyte flow
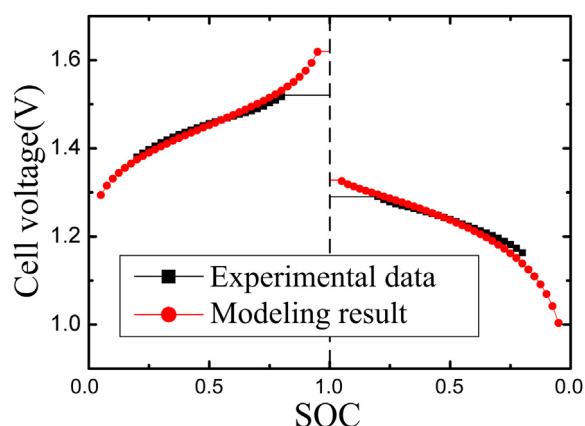
Fig. 4. Comparison between the modeling results and experimental data.

throughout the channel and electrode domains. The fluid pressure uniformly decreases from the inlet channel to the outlet one in single-inlet design, while in multi-inlet design, the pressure decreases rapidly near the side inlet due to the penetration of the flow through the porous media. In addition, the fluid pressure drop of single-inlet design is about 50% higher than that of multi-inlet design under the same flow rate boundary condition.

The electric potential distribution of electrode, which reflects the local cell performance, may vary with the operation condition and geometric structure of VRB cell. Figs. 7 and 8 show the electric potential distributions of single-inlet and multi-inlet cells during discharge process, respectively. In the single-inlet cell, electric potential uniformly distributes along the Z axis, while for the multi-inlet one, the electrical potential of the outlet region is about 20 mV less than that of its inlet counterpart. It should be noted that for the two inlet designs, the voltage drops between the porous electrode and current collector are both around 20 mV.

In order to reveal the root causes of the inlet design effects on cell performance, the overpotential distributions at electrode cross-sections for single-inlet and multi-inlet designs are shown in Figs. 9 and 10, respectively. The distribution patterns of overpotential for positive and negative electrodes are almost mirror-symmetric. The absolute value of overpotential of negative electrode is about three
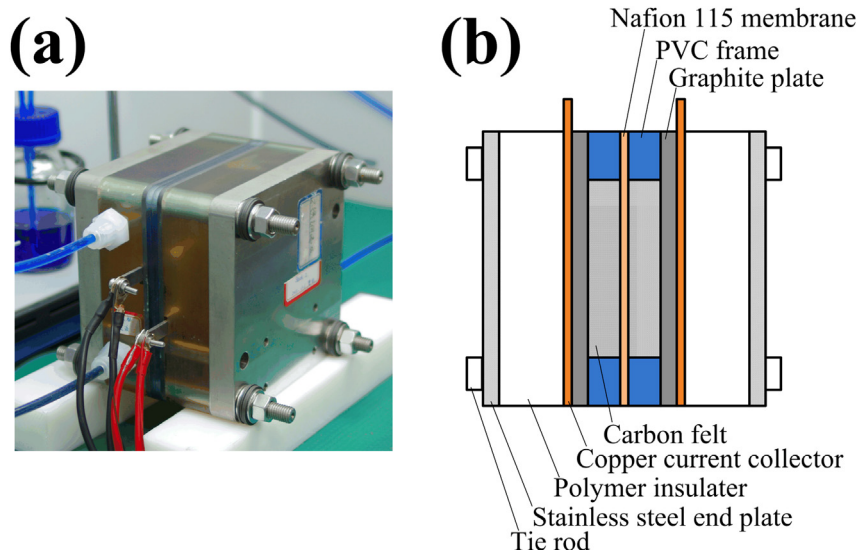
Fig. 3. (a) Photo of the assembled single cell. (b) A side view of the cell structure.

Table 3
Model accuracy analysis under various *soc* values.

soc	Voltage during discharge			Voltage during charge		
	Experimental (V)	Modeling (V)	Difference %	Experimental (V)	Modeling (V)	Difference %
0.2	1.163	1.139	2.06	1.380	1.374	0.43
0.3	1.196	1.181	1.25	1.412	1.404	0.57
0.4	1.218	1.212	0.49	1.436	1.429	0.49
0.5	1.238	1.237	0.08	1.455	1.452	0.21
0.6	1.256	1.258	0.16	1.472	1.475	0.20
0.7	1.270	1.277	0.55	1.489	1.500	0.74
0.8	1.290	1.295	0.39	1.517	1.531	0.92
Average	1.233	1.228	0.71	1.451	1.452	0.51

to five times as high as that of positive electrode, because the electrochemical activity for VO^{2+}/VO_2^+ transformation is much higher than that for V^{2+}/V^{3+} transformation. The overpotential distribution at the cross-section of the electrode remains almost unchanged along the *Z* axis in the single-inlet design, while the distribution pattern varies significantly from inlet to outlet portions for multi-inlet design.

The distinct distributions of electrolyte pressure for the two inlet designs are considered to be the main factor that accounts for the overpotential variations mentioned above. At a relatively low

electrolyte flow rate, such as *stoich* of 10, the electrochemical reaction rate is controlled by the convective diffusion of ionic reactants, which is determined by the local velocity of electrolyte fluid. With more sufficient supply of ionic reactants, the transform of vanadium ions processes faster, resulting in a greater absolute value of overpotential in the porous electrode. For single-inlet design, electrolyte flow distribute evenly in both flow channel and porous electrode, leading to uniform overpotential distributions given in Fig. 9. For multi-inlet design, the electrolyte flow penetrates into porous electrode through side inlet and then
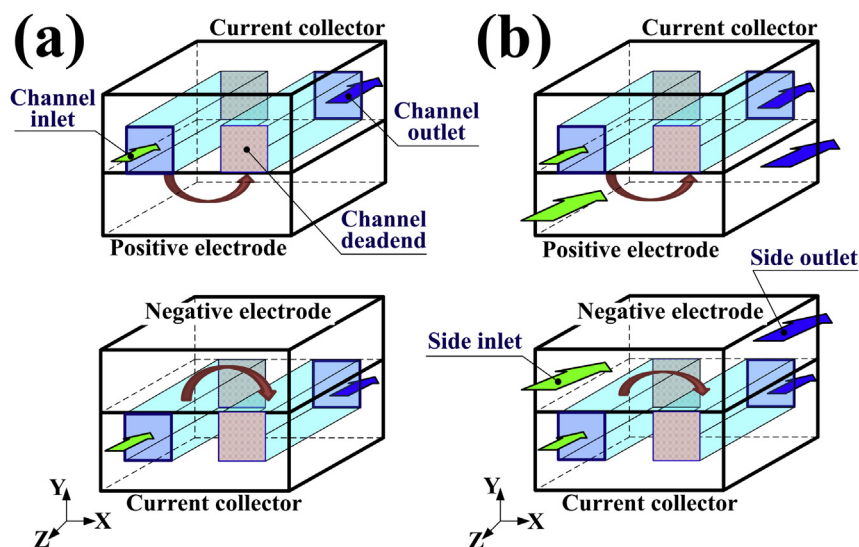

Fig. 5. Schematic of electrolyte flow path inside the cell for (a) single-inlet design and (b) multi-inlet design. Green and blue arrows indicate electrolyte's inlet and outlet flow directions, respectively, while brown arrows represent possible flow paths through the porous electrode. (For interpretation of the references to color in this figure legend, the reader is referred to the web version of this article.)
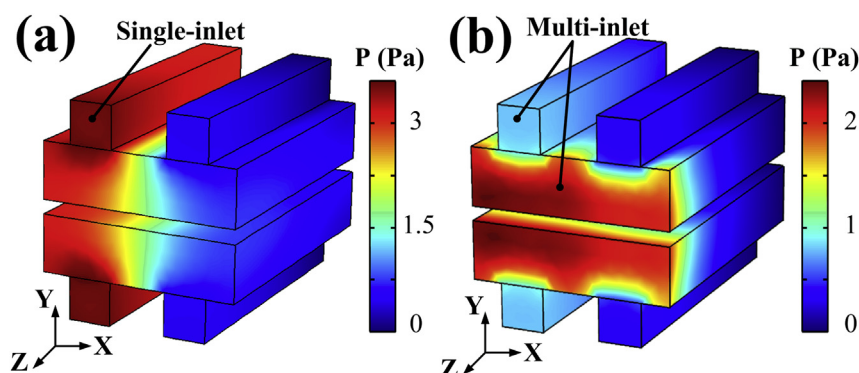

Fig. 6. Fluid pressure distributions of the interdigitated flow channel model at *stoich* of 10. (a) Single-inlet design, (b) multi-inlet design.
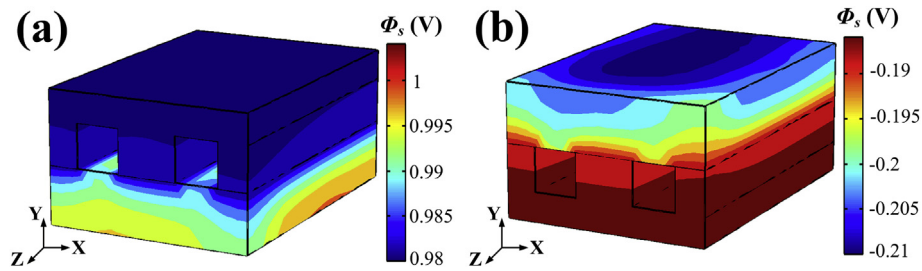
Fig. 7. Electric potential distributions of electrodes during discharge at *stoich* of 10 for single-inlet design. (a) Positive electrode; (b) negative electrode.
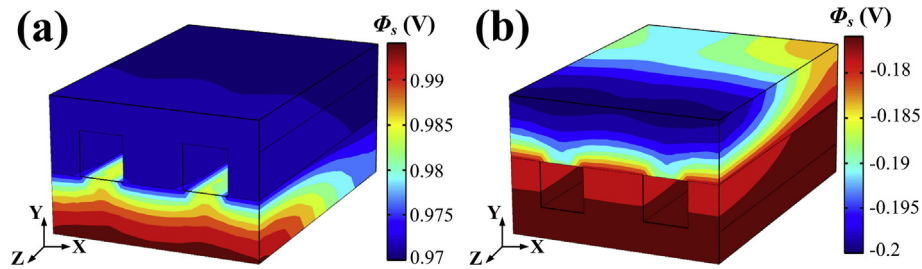

Fig. 8. Electric potential distributions of electrodes during discharge at *stoich* of 10 for multi-inlet design. (a) Positive electrode; (b) negative electrode.

processes the channel-to-channel path around the outlet portion, resulting in uneven overpotential distribution shown in Fig. 10.

3.3. Flow rate effects on cell performance

Flow rate of electrolyte solution is another key factor affecting cell performance. Figs. 11 and 12 show quantitative results of electric potential difference between certain points at inlet and outlet for single-inlet and multi-inlet designs as flow rate varies. For the positive half-cell, potential differences between point A1 and A2 at electrode/membrane interface, B1 and B2 at electrode/current collector interface, and C1 and C2 at the edge of current collector are calculated. Same calculations are also carried out for the negative half-cell. For single-inlet design, all the potential differences between inlet and outlet are less than 3 mV, while for multi-inlet design, absolute values of electric potential difference near the membrane are about 20 mV higher than those around current collectors at *stoich* of 10 and the gaps decline to about 5 mV

as *stoich* increases to 100. The profiles of electric potential difference at various *stoichs* can be attributed to the different convective diffusion behaviors of ionic reactants, which are dominated by velocity distribution of electrolyte, as stated above.

As is known to all, the electrochemical reaction rate of porous electrode, which determines the VRB cell performance, is mainly controlled by three factors: reactivity of the electrode, mass transfer of ionic reactants and utilized reaction sites of porous electrode. Fig. 13 shows cell voltage profiles with electrolyte flow rates in single-inlet and multi-inlet designs. Cell voltages are enhanced by about 5% for single-inlet design and 10% for multi-inlet design, respectively, as *stoich* increases from 5 to 25. But the voltage improvement is less than 1% for both designs when *stoich* is higher than 25. The effect of flow rate on cell voltage indicates that the ionic convective diffusion is the dominating factor for VRB performance at lower electrolyte *stoich*. At higher *stoich*, however, the electrochemical reaction rate is controlled by other factors such as electrode reactivity and reactive surface area rather than
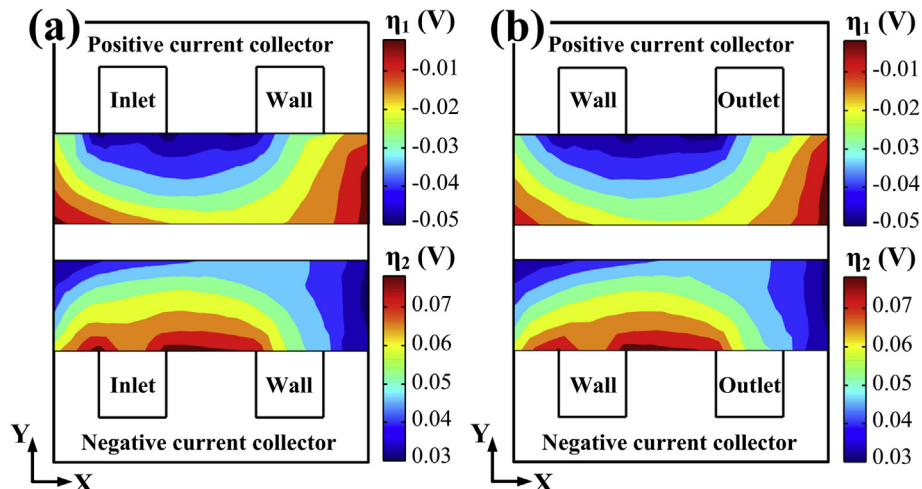

Fig. 9. Overpotential distributions for single-inlet design during VRB discharge at *stoich* of 10. (a) Inlet cross-section at *Z* of 0 mm; (b) outlet cross-section at *Z* of −10 mm.
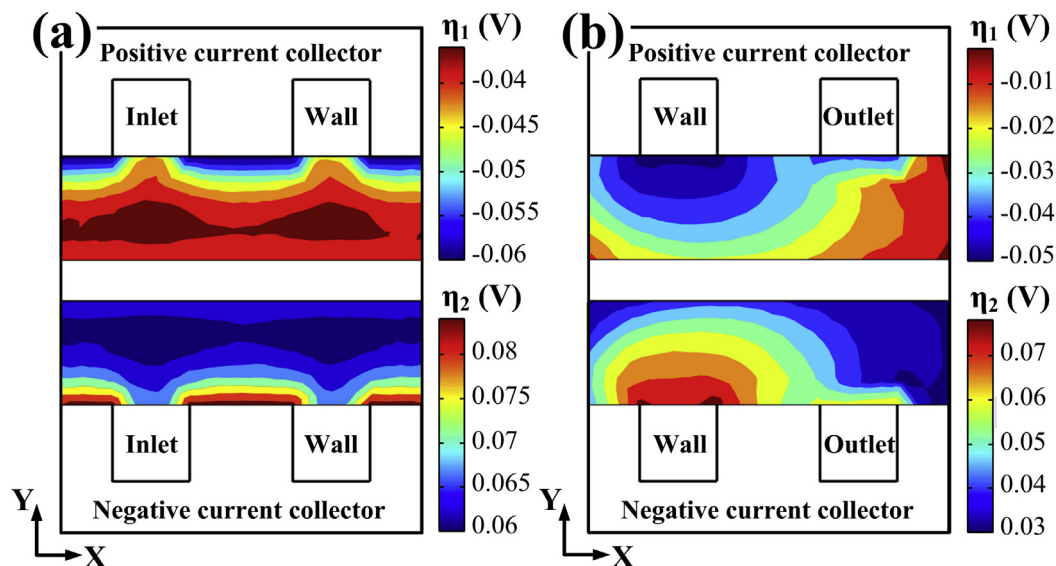
Fig. 10. Overpotential distributions for multi-inlet design during VRB discharge at *stoich* of 10. (a) Inlet cross-section at *Z* of 0 mm; (b) outlet cross-section at *Z* of −10 mm.

convective mass transfer. From system design aspect, higher electrolyte *stoich* will cause more power consumption of liquid pumps, resulting in lower system efficiency. Therefore, the relationship between VRB cell performance and electrolyte flow rate discussed above will provide additional electrochemical reaction information for robust system design.

In addition to the cell voltage growth with increasing *stoich*, comparison of VRB cell performance for single-inlet and multi-inlet designs at various electrolyte flow rates is also discussed. Single-inlet cell performs better than the multi-inlet one at *stoich* less than 25, but the result is reversed at *stoich* higher than 25, which is shown in Fig. 13. Electrolyte of single-inlet cell maintains uniform
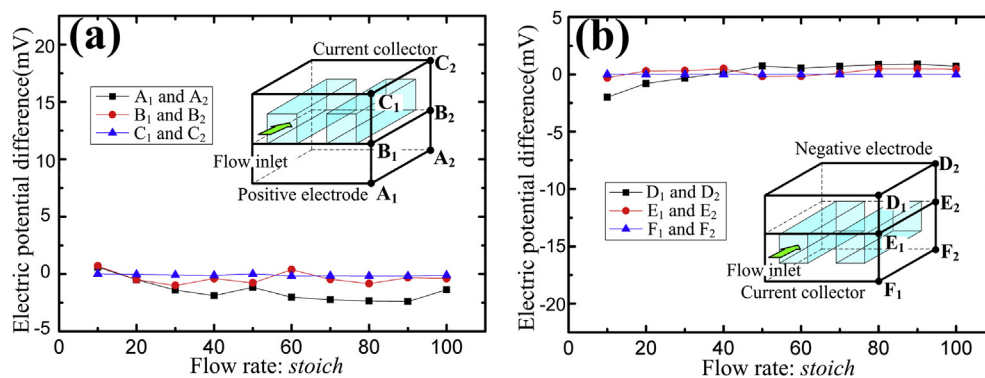

Fig. 11. Electric potential difference between the inlet and outlet portions of VRB cell as the function of electrolyte flow rate for single-inlet design. (a) Positive half-cell, (b) negative half-cell. A to F indicates the cell's different inlet and outlet locations.
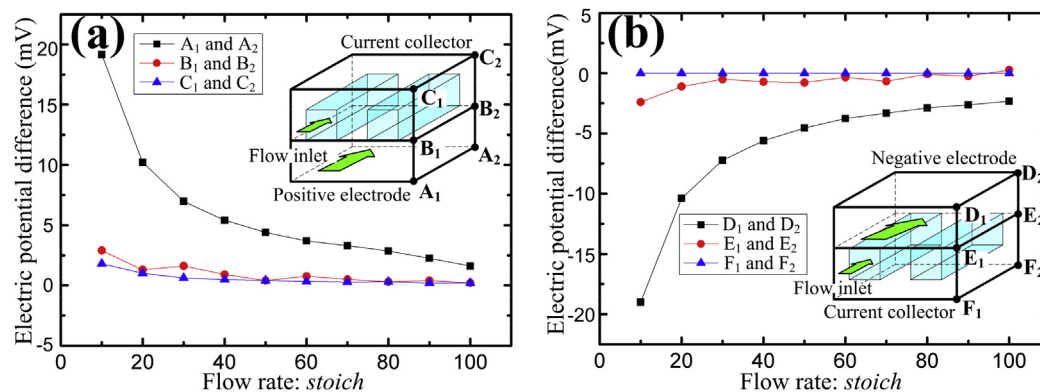

Fig. 12. Electric potential difference between the inlet and outlet portions as the function of electrolyte flow rate for multi-inlet design. (a) Positive half-cell, (b) negative half-cell. A to F indicates the cell's inlet and outlet different locations.
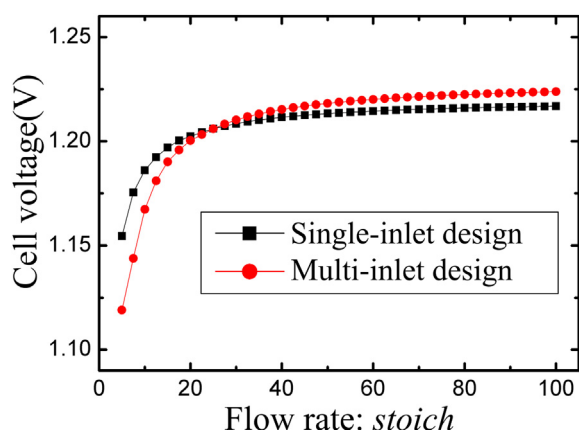
Fig. 13. Cell voltage as the function of electrolyte flow rate during VRB discharge. (a) Single-inlet design; (b) multi-inlet design.

distribution along the Z axis at low flow rates, while the fluid pressure drops rapidly at the side inlet portion for multi-inlet cell. As a result, most of the porous electrode other than the inlet portion for multi-inlet cell is much less utilized than that of the single-inlet one and thus represents lower cell voltage. At high flow rates, both designs show uniform electrolyte distribution, so the dominating factor for cell performance is utilization ratio of porous electrode rather than convective diffusion of ionic reactants. The extra side manifold of multi-inlet design provides an additional electrolyte flow path, leading to higher utilization of reactive sites for porous electrode and hence the better performance.

3.4. Effects of channel dimensions

Channel dimension of the current collector is another important parameter for cell performance which greatly affects distributions of current density and fluid flow. As shown in Fig. 14, the current density distribution of solid phase differs between the two cell designs. For multi-inlet design, current density around side inlet is much higher than that near the side outlet, while the difference is not obvious for single-inlet design. In addition, the current density of porous electrode at current collector side is much higher than the value at membrane side, contributed from the ohmic effects of electric conduction in porous electrodes and ionic conduction in electrolyte solutions [1].

Fig. 15 shows cell voltage profiles with varied land widths under certain operating conditions for the two inlet designs at *stoich* of 10. As land width increases, cell voltage rises until a plateau is reached

which locates at 3 mm for channel cross-section of 1.5×1.5 mm and 5 mm for 1.0×1.0 mm. The variations of land width will affect both the transportation of reactants inside the porous electrode and the electronic conduction of the current collector. With increased land width, the distribution of electrolyte fluid velocity becomes more uniform and the magnitude of velocity shows greater value. As a result, the efficient convective transportation of ionic reactants improves cell performance. Besides, the increase of land width also improves the electronic conduction due to the enlarged contact area between electrode and current collector. It is noted that the single-inlet cell performs better than the multi-inlet one with larger channel size while the results is reversed for smaller channel size, as shown in Fig. 15. As the cross-section area of channel varies from 2.25 mm^2 to 1 mm^2, cell voltage maintains almost unchanged for single-inlet cell while it is about 40 mV increase for multi-inlet cell. For single-inlet design, the electrolyte solution flows from the inlet channel to the outlet one through the porous electrode uniformly and the cross-section of channel shows little effect on the flow distribution of the cell and its performance as well. While for multi-inlet design, electrolyte solution mainly flows into channel with larger cross-section area, but the side inlet becomes dominating electrolyte flow path when the cross-section area is smaller. As a result, with a smaller channel cross-section area such as 1 mm^2, the multi-inlet cell gains more efficient utilization of porous electrode for electrochemical reaction than that of single-inlet cell, leading to its higher cell voltage.

3.5. Model analysis and application

The proposed 3D model of VRB is based on the coupling of fluid dynamics, mass transfer mechanism and electrochemistry. The model accuracy is validated by comparing with the experimental results as discussed in Section 3.1. Effects of varied parameters on model output have been fully discussed in Sections 3.2–3.4. Similar studies have also been carried out by other scientists [1,25–30]. In this part, we focus on effects of enlarged geometric parameters on the model accuracy, as dimensions of real VRB cell stack are much larger than those used in this model.

Taking discharge process at *stoich* of 80 and current density of 60 mA/cm^2 for example, performance of multi-inlet cell (Cell-1) with dimensions given in Table 1 is compared with cells of enlarged width and length respectively, as shown in Fig. 16. With the same channel length of 10 mm, Cell-2 and Cell-3 increase electrode width up to 35 mm and 70 mm by raise the number of channels, while Cell-4 and Cell-5 increase channel lengths up to 50 mm and 100 mm. The results show that the effect of geometric dimension increment on modeling accuracy is less than 0.5%. Although voltage
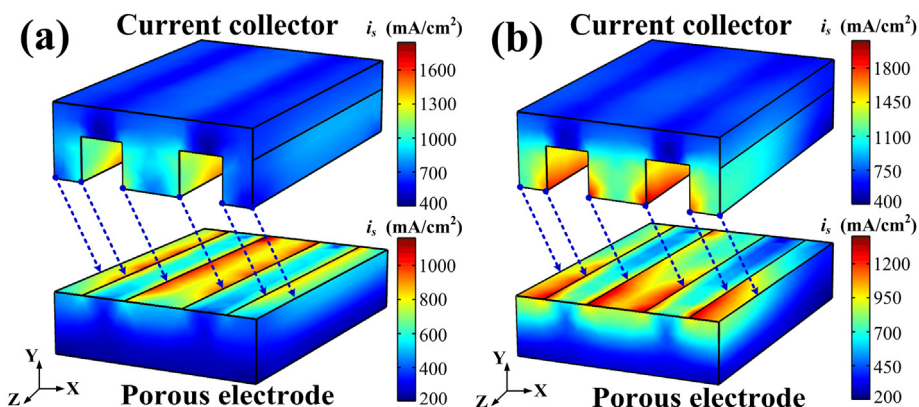

Fig. 14. Current density distributions of electrode and current collector during VRB discharge at *stoich* of 10. (a) Single-inlet design; (b) multi-inlet design.
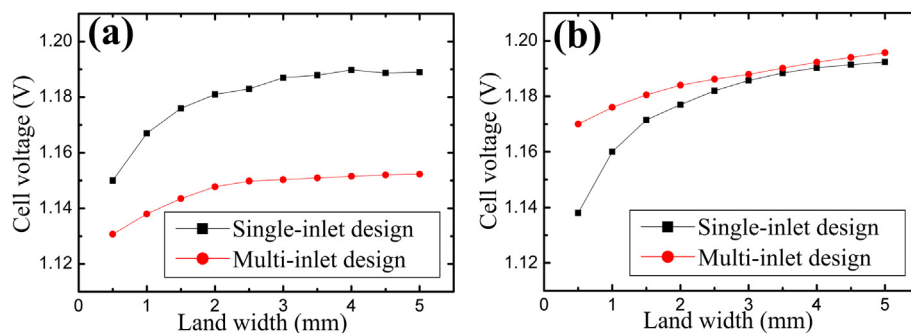
Fig. 15. Cell voltage as a function of flow field land width during VRB discharge for single-inlet and multi-inlet cells at electrolyte *stoich* of 10. (a) Channel width and height are both 1.5 mm; (b) channel width and height are both 1 mm.

difference at low *soc* during discharge may reach 2.5%, the effects of enlarged dimensions on model accuracy could be neglected for the mid-range of *soc* in which VRB system mainly operates for application.

As well known, the area of membrane and electrode in VRB cell stack used for energy storage system could be as large as hundreds of square centimeters, but their thicknesses are in the scale of micrometers to millimeters. Therefore the finite element mesh built with such geometry may lead to tremendous computational calculations and it is difficult to propose a perfect coupled model achieving convergence with such a huge number of mesh elements. The proposed 3D model can study VRB cells with enlarged dimensions more efficiently while preserving accuracy. With this

model, electrochemical performance and fluid pressure drop could be calculated effectively with various VRB cell geometric parameters, such as manifold structure and flow channel dimensions, which are crucial parameters to the cell stack design. In addition, the effects of operating conditions on cell performance were also studied. The results could direct the optimization of VRB system operation strategy.

4. Conclusion

A 3D model of VRB cell with interdigitated flow channel design has been developed in the paper. Based on the coupled modeling of flow field structures and electrochemical reactions, VRB cells with
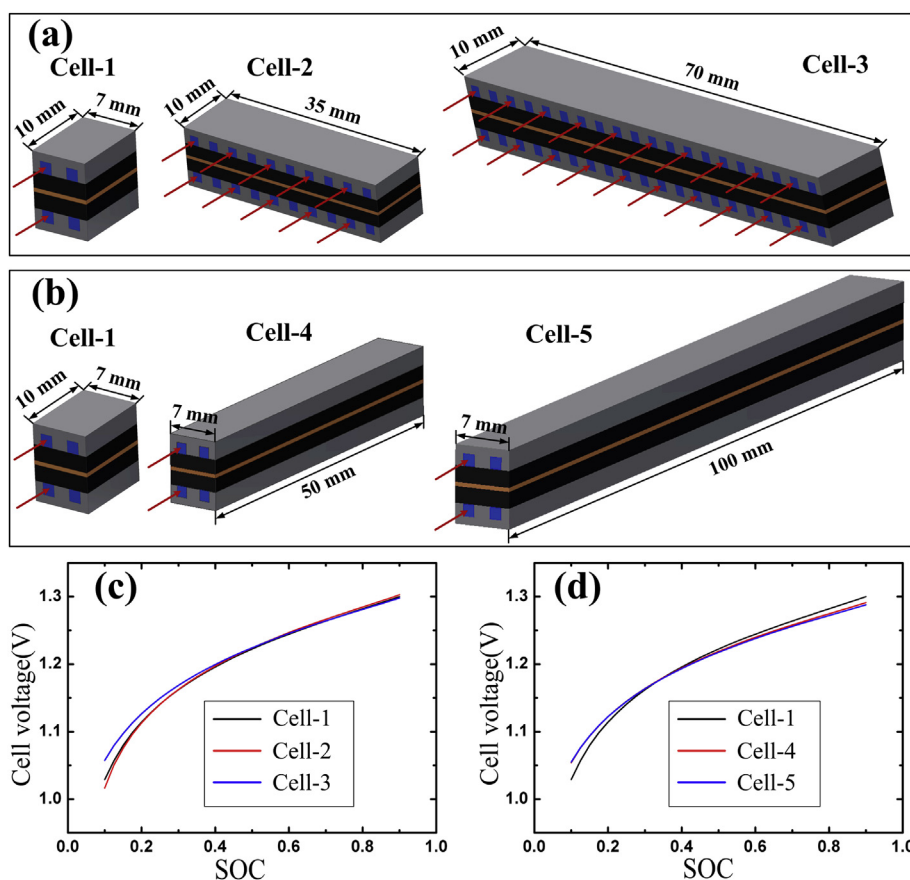

Fig. 16. Model accuracy analysis with enlarged cell geometric dimensions for multi-inlet design during discharge at *stoich* of 80 and current density of 60 mA/cm². (a) and (b) depict increasing dimensions for width and length, respectively, while red arrows indicating fluid direction at inlet channel. (c) and (d) show modeling results with varied cell widths and lengths, respectively. (For interpretation of the references to color in this figure legend, the reader is referred to the web version of this article.)

two different inlet designs have been constructed and cell performance is discussed in terms of inlet manifold's geometry, electrolyte flow rates and channel dimensions. For the single-inlet design, the electrolyte flow field, electrical potential, current density and overpotential uniformly distribute along the flow direction of electrolyte with varied electrolyte flow rates and channel dimensions. For the multi-inlet design, the pressure of electrolyte drops significantly in the side inlet of porous electrode at low flow rates (*stoich* less than 25), resulting in uneven distributions of electrolyte flow field and cell potential. At higher electrolyte flow rates (*stoich* more than 25), the potential distribution of the multi-inlet cell becomes uniform and the utilization of porous electrode is more efficient than that of the single-inlet cell, leading to a better cell performance. For both designs, cell voltage rises until a plateau is reached as land width increases.

The 3D model can be employed to optimize both VRB stack design and system operation conditions. Literature and our laboratory results show that other factors such as *soc*, current density and electrode properties also have a significant impact on cell performance, and they will be taken into account in the future work.

Acknowledgment

References

[1] Vynnycky M. Analysis of a model for the operation of a vanadium redox battery. Energy 2011;36:2242—56.

[2] Sum E, Rychcik M, Skyllas-Kazacos M. Investigation of the V(V)/V(IV) system for use in the positive half-cell of a redox battery. J Power Sources 1985;16:85—95.

[3] Skyllas-Kazacos M, Rychcik M, Robins R, Fane AG, Green MA. New all-vanadium redox flow cell. J Electrochem Soc 1986;133:1057—8.

[4] Schreiber M, Harrer M, Whitehead A, Bucsich H, Dragschitz M, Seifert E, Tymciw P. Practical and commercial issues in the design and manufacture of vanadium flow batteries. J Power Sources 2012;206:483—9.

[5] Ferreira HL, Garde R, Fulli G, Kling W, Lopes JP. Characterization of electrical energy storage technologies. Energy 2013;53:288—98.

[6] Howlader AM, Izumi Y, Uehara A, Urasaki N, Senjyu T, Yona A, Saber AY. A minimal order observer based frequency control strategy for an integrated wind-battery-diesel power system. Energy 2012;46:168—78.

[7] Tana CW, Green TC, Hernandez-Aramburo CA. A stochastic method for battery sizing with uninterruptible-power and demand shift capabilities in PV (photovoltaic) systems. Energy 2010;35:5082—92.

[8] Arun P, Banerjee R, Bandyopadhyay S. Optimum sizing of battery-integrated diesel generator for remote electrification through design-space approach. Energy 2008;33:1155—68.

[9] Virulkar V, Aware M, Kolheb M. Integrated battery controller for distributed energy system. Energy 2011;36:2392—8.

[10] Olabi AG. State of the art on renewable and sustainable energy. Energy 2013;61:2—5.

[11] Moghaddam AA, Seifi A, Niknam T, Pahlavani MRA. Multi-objective operation management of a renewable MG (micro-grid) with back-up micro-turbine/fuel cell/battery hybrid power source. Energy 2011;36:6490—507.

[12] Zhang XW, Tan SC, Li GJ, Li J, Feng ZP. Components sizing of hybrid energy systems via the optimization of power dispatch simulations. Energy 2013;52:165—72.

[13] Østergaard PA. Reviewing optimisation criteria for energy systems analyses of renewable energy integration. Energy 2009;34:1236—45.

[14] Dargahi V, Sadigh AK, Pahlavani MRA, Shoulaie ADC. (direct current) voltage source reduction in stacked multicell converter based energy systems. Energy 2012;46:649—63.

[15] Dell RM, Rand DAJ. Energy storage — a key technology for global energy sustainability. J Power Sources 2001;100:2—17.

[16] Skyllas-Kazacos M, Kazacos M. State of charge monitoring methods for vanadium redox flow battery control. J Power Sources 2011;196:8822—7.

[17] Zhao P, Zhang HM, Zhou HT, Chen J, Gao SJ, Yi BL. Characteristics and performance of 10 kW class all-vanadium redox-flow battery stack. J Power Sources 2006;162:1416—20.

[18] Zhao P, Zhang HM, Zhou HT, Yi BL. Nickel foam and carbon felt applications for sodium polysulfide/bromine redox flow battery electrodes. Electrochim Acta 2005;51:1091—8.

[19] Zhou HT, Zhang HM, Zhao P, Yi BL. A comparative study of carbon felt and activated carbon based electrodes for sodium polysulfide/bromine redox flow battery. Electrochim Acta 2006;51:6304—12.

[20] Han PX, Wang HB, Liu ZH, Chen X, Ma W, Yao JH, Zhu YW, Cui GL. Graphene oxide nanoplatelets as excellent electrochemical active materials for VO^{2+}/VO_2^+ and V^{2+}/V^{3+} redox couples for a vanadium redox flow battery. Carbon 2011;49:693—700.

[21] Aaron DS, Liu Q, Tang Z, Grim GM, Papandrew AB, Turhan A, Zawodzinski TA, Mench MM. Dramatic performance gains in vanadium redox flow batteries through modified cell architecture. J Power Sources 2012;206:450—3.

[22] Li S, Huang KL, Liu SQ, Fang D, Wu XW, Lu D, Wu T. Effect of organic additives on positive electrolyte for vanadium redox battery. Electrochim Acta 2011;56:5483—7.

[23] Gattrell M, Park J, MacDougall B, Apte J, McCarthy S, Wu CW. Study of the mechanism of the vanadium 4+/5+ redox reaction in acidic solutions. J Electrochem Soc 2004;151:A123—30.

[24] Vijayakumar M, Li LY, Graff G, Liu J, Zhang HM, Yang ZG, Hu JZ. Towards understanding the poor thermal stability of V^{5+} electrolyte solution in vanadium redox flow batteries. J Power Sources 2011;196:3669—72.

[25] Shah AA, Tangirala R, Singh R, Wills RGA, Walsh FC. A dynamic unit cell model for the all-vanadium flow battery. J Electrochem Soc 2011;158:A671—7.

[26] Shah AA, Watt-Smith MJ, Walsh FC. A dynamic performance model for redox-flow batteries involving soluble species. Electrochim Acta 2008;53:8087—100.

[27] Shah AA, Al-Fetlawi H, Walsh FC. Dynamic modelling of hydrogen evolution effects in the all-vanadium redox flow battery. Electrochim Acta 2010;55:1125—39.

[28] Al-Fetlawi H, Shah AA, Walsh FC. Modelling the effects of oxygen evolution in the all-vanadium redox flow battery. Electrochim Acta 2010;55:3192—205.

[29] Al-Fetlawi H, Shah AA, Walsh FC. Non-isothermal modelling of the all-vanadium redox flow battery. Electrochim Acta 2009;55:78—89.

[30] You DJ, Zhang HM, Chen J. A simple model for the vanadium redox battery. Electrochim Acta 2009;54:6827—36.

[31] Tang A, Ting S, Bao J, Skyllas-Kazacos M. Thermal modelling and simulation of the all-vanadium redox flow battery. J Power Sources 2012;203:65—76.

[32] Xu Q, Zhao TS, Leung PK. Numerical investigations of flow field designs for vanadium redox flow batteries. Appl Energy 2013;105:47—56.